Science

AAAS

Mars North Polar Deposits: Stratigraphy, Age, and Geodynamical Response
Roger J. Phillips, *et al.*
Science **320**, 1182 (2008);
DOI: 10.1126/science.1157546

Mars North Polar Deposits: Stratigraphy, Age, and Geodynamical Response

Roger J. Phillips,[1,2]* Maria T. Zuber,[3] Suzanne E. Smrekar,[4] Michael T. Mellon,[5] James W. Head,[6] Kenneth L. Tanaka,[7] Nathaniel E. Putzig,[1] Sarah M. Milkovich,[4] Bruce A. Campbell,[8] Jeffrey J. Plaut,[4] Ali Safaeinili,[4] Roberto Seu,[9] Daniela Biccari,[9] Lynn M. Carter,[8] Giovanni Picardi,[9] Roberto Orosei,[10] P. Surdas Mohit,[11,12] Essam Heggy,[13,14] Richard W. Zurek,[4] Anthony F. Egan,[1] Emanuele Giacomoni,[9] Federica Russo,[9] Marco Cutigni,[9] Elena Pettinelli,[15] John W. Holt,[16] Carl J. Leuschen,[17] Lucia Marinangeli[18]

The Shallow Radar (SHARAD) on the Mars Reconnaissance Orbiter has imaged the internal stratigraphy of the north polar layered deposits of Mars. Radar reflections within the deposits reveal a laterally continuous deposition of layers, which typically consist of four packets of finely spaced reflectors separated by homogeneous interpacket regions of nearly pure ice. The packet/interpacket structure can be explained by approximately million-year periodicities in Mars' obliquity or orbital eccentricity. The observed ~100-meter maximum deflection of the underlying substrate in response to the ice load implies that the present-day thickness of an equilibrium elastic lithosphere is greater than 300 kilometers. Alternatively, the response to the load may be in a transient state controlled by mantle viscosity. Both scenarios probably require that Mars has a subchondritic abundance of heat-producing elements.

The north polar region of Mars is part of an immense sedimentary basin that records over 3 billion years of deposition and erosion of ice, dust, lava, and other lithic material of varying composition and includes the plateau of Planum Boreum, covering an area of ~800,000 km^2. Beneath a thin residual cap of bright, nearly pure water ice, the north polar layered deposits (as a single unit: NPLD) (1) make up the bulk of Planum Boreum and are probably the result of cyclical variations in the orbit and rotation of Mars that affected insolation at the poles and elsewhere. The layering results largely from different fractions of dust and ice (2, 3), which affect the visible-wavelength albedo. In the last decade, high-resolution images have revealed a basal unit (BU) (4) beneath the NPLD. The BU is considerably different than the NPLD (5–7), principally in its lower albedo, but it also has thicker layers (8). Images show that outcrops in the upper portions of the BU sometimes display a platy, interbedded sequence of ice-rich and sand-rich layers (9).

Understanding the origin and evolution of both the NPLD and the BU will provide important information on the recent climate history of Mars. These deposits also act as loads on the underlying lithosphere, and the amount of downward deflection of the substrate constrains the thermal and rheological state of the present-day martian interior. The Shallow Radar (SHARAD) and Mars Advanced Radar for Subsurface and Ionospheric Sounding (MARSIS) [see supporting online material (SOM) text] penetrate these deposits, providing a three-dimensional view of north polar stratigraphy and the deformation of its base. Here we present results from these radar sounders and discuss the genesis and evolution of these north polar units, the relation of these deposits to climate signals, and the geodynamical state of the interior.

Radar stratigraphy. Figure 1 shows a radargram of a SHARAD traverse (orbit 5192) across Planum Boreum, from the outlying plateau of Olympia Planum near 140°E to the minor lobe of Planum Boreum, Gemina Lingula, near 5°E. Here, radar reflections arise from boundaries between layers differing in their fractions of ice, dust, and sand. The radar reflections in Planum Boreum are closely spaced to a depth of ~500 m and then are more widely spaced at greater depths, though they are clustered into distinct packets of reflectors. The volume containing all of these reflectors corresponds to the NPLD, whereas the diffusely reflective zone below ~2 km of depth (mostly absent under Gemina Lingula) corresponds to the BU. Orbit 5192 crosses a number of spiral troughs that are up to several hundred meters deep. The troughs interrupt the shallow radar reflectors, though the timing of layer deposition and trough formation is ambiguous (10).

Mapping of BU exposures in chasmata on the periphery of Planum Boreum led to the hypothesis that the BU is absent beneath Gemina Lingula (5, 6) and that the NPLD here rests directly on the few-billion-year-old Vastitas Borealis Formation (VBF) of largely sedimentary origin; our examination of many SHARAD tracks across Planum Boreum confirms this hypothesis and shows that the BU is largely confined to the major lobe of Planum Boreum. Additionally, where the radar-mapped BU unambiguously intersects the floor of Chasma Boreale, BU is observed in those locales in surface images. A radargram from SHARAD orbit 5220 (Fig. 2) shows that in this locale the BU actually extends across Chasma Boreale, where it is exposed in the walls and forms a bench on the Gemina Lingula side before terminating abruptly. The BU increases to a thickness of ~1000 m beneath the highest portions of Planum Boreum, whereas the NPLD has a roughly constant thickness, except near its boundaries. Thus, elevation variations across Planum Boreum are largely attributable to thickness variations in the BU, and it follows that depositional and erosional processes have been largely uniform across the cap since the bottommost layers of the NPLD were emplaced. This conclusion is corroborated by the observation that some of the stronger radar reflectors can be traced completely across the cap (Fig. 1), a distance of nearly 1000 km.

SHARAD signals locally penetrated the BU to reveal a substrate reflection (presumably the top of the VBF), but this reflection in many places is obscured by volume scattering of the radar waves within the BU (Fig. 1). The BU does show internal reflectors, as expected from limited surface exposures of this unit (8). The substrate reflector can be traced ~100 km beneath Olympia Planum in Fig. 1, which implies that the material making up the bulk of Olympia Planum was deposited on a common substrate with the BU. The lower-frequency MARSIS radar, which is able to penetrate more deeply and is apparently less sensitive to volume scattering, shows these relations more clearly (fig. S1). As projected in earlier work (6), the SHARAD results show that the maximum thickness of the BU beneath the NPLD is approximately the elevation of Olympia Planum above its lowland surroundings, suggesting a common link. However, the BU appears to terminate on the boundary of Planum Boreum, lacking continuity with Olympia Planum (Fig. 1). The substrate beneath the NPLD and the BU is remarkably flat, showing essentially no deflection from the mass load of the polar deposits. This lack of deflection was noted in an early MARSIS radar profile, but low range resolution provided only a crude bound on elastic lithosphere thickness (11), whereas SHARAD data place tighter geodynamical constraints because of the instrument's superior range resolution.

SHARAD data for Orbit 5297 (Fig. 3) show more detail in the Gemina Lingula region. The marked flatness of the basal interface is apparent, as is a repetition of the fine-scale layering observed at

[1]Southwest Research Institute, Boulder, CO 80302, USA. [2]Washington University, St. Louis, MO 63101, USA. [3]Massachusetts Institute of Technology, Cambridge, MA 02139–4307, USA. [4]Jet Propulsion Laboratory, California Institute of Technology, Pasadena, CA 91109, USA. [5]University of Colorado, Boulder, CO 80309–0392, USA. [6]Brown University, Providence, RI 02912, USA. [7]U.S. Geological Survey, Flagstaff, AZ 86001, USA. [8]Smithsonian Institution, Washington, DC 20013–7012, USA. [9]Dipartimento InfoCom, Università di Roma "La Sapienza," I-00184 Rome, Italy. [10]Istituto Nazionale di Astrofisica, I-00133 Rome, Italy. [11]Scripps Institution of Oceanography, La Jolla, CA 92093, USA. [12]University of British Columbia, Vancouver, British Columbia, Canada, V6T 1Z4. [13]Lunar and Planetary Institute, Houston, TX 77058, USA. [14]Institute de Physique du Globe de Paris, Paris, France. [15]Università Roma Tre, 00146 Rome, Italy. [16]Jackson School of Geosciences, University of Texas, Austin, TX 78712, USA. [17]University of Kansas, Lawrence, KS 66045–7612, USA. [18]Universita' d'Annunzio 65127 Pescara, Italy.

*To whom correspondence should be addressed. E-mail: roger@boulder.swri.edu

the surface. Separated by interpacket regions of few reflections, there are four such layer packets of closely spaced reflections (also seen in Fig. 1), whose signal strength becomes weaker at depth, as expected (fig. S2). Inspection of other radargrams confirms the persistence of four packet structures across the cap, with local variation due to heterogeneous erosion and deposition leading in places to missing packets or extra packets (for instance, Fig. 3, bottom center). This packet/interpacket structure represents a second, larger scale of layering in addition to the finer-scale reflectors within the packets.

The observed dielectric transparency of the NPLD to radar waves in the frequency band for SHARAD (Figs. 1 and 3) and also for MARSIS data (11) implies that the amount of dust in the total NPLD column must be small: Electrical loss is high in non-ice analog materials (fig. S3) and in SHARAD non-ice targets on Mars. A low dust content is consistent with spectral mapping (12, 13), which has shown that ice dominates the NPLD, and by analogy with a bulk density estimate of the south polar layered deposits (SPLD) (14). Following a well-established approach (15), we found that the weakest reflectors detected by SHARAD could be ice layers as thin as 10 cm containing ~10% dust or 1-m-thick layers containing only ~2% dust. The strongest reflectors can be explained by a 2-m layer of ice containing ~30%

dust. We conclude that reflections from within the packets are caused by variations of small dust fractions contaminating an ice matrix, and that the relatively homogeneous interpacket regions are largely ice with a minimal dust component.

Climate implications. Three well-understood orbital and rotational periodicities affect insolation at Mars' poles (16): (i) an obliquity variation (120,000 years), (ii) a climatic precession (17) (51,000 years), and (iii) an eccentricity variation (95,000 to 99,000 years); the first has the largest influence on martian climate (18). It has long been held that fine-scale layering observed in images of the NPLD is tied somehow to these climate forcings (2). The fine-scale intrapacket reflections revealed by SHARAD may also be tied to one or more of these periodicities, but it is clear that the radar cannot resolve the finest scale of layering observed in images and that some of this layering is related to surficial processes alone (9). The actual layering, whether observed in images or radargrams, cannot yet be uniquely tied to specific climate forcings, and the finest scale of layering could conceivably reflect individual, very intense dust storms. Because physical layers mapped by SHARAD are continuous laterally up to 1000 km, whatever mechanisms that were operating to create layering must have been homogeneous over that scale, and climate forcing is the leading candidate. The packets

represent widespread processes that added and removed ice, added dust, and concentrated dust during times of ice sublimation because the mere presence of radar reflections of variable strength almost certainly requires the ice/dust ratio to vary with depth. Climate modeling suggests that the NPLD postdates the last transition from high to low mean obliquity (LMO) ~5 million years ago (Ma), before which ice at the pole was unstable against complete loss by sublimation (19). This conclusion is consistent with several results that correlate variations in depth-dependent layer brightness with the time series of an insolation model (16, 20), but it is not possible to establish this connection uniquely at present.

From the SHARAD constraints, the three regions between the packets with few radar reflections represent times of substantial ice deposited at the pole and/or little dust delivered to the pole. One simple model that yields the packet/interpacket structure is a variable dust supply over a background of overall ice growth during the last ~5 million years (My). Dust storms may be more prevalent during high obliquity at solstice (21), and this effect is probably enhanced at times of high eccentricity; conversely, at low obliquities and eccentricities, dust storm activity and intensity should diminish (22). Packets could form during times of high obliquity (and eccentricity), and sublimation events during short-period excursions in
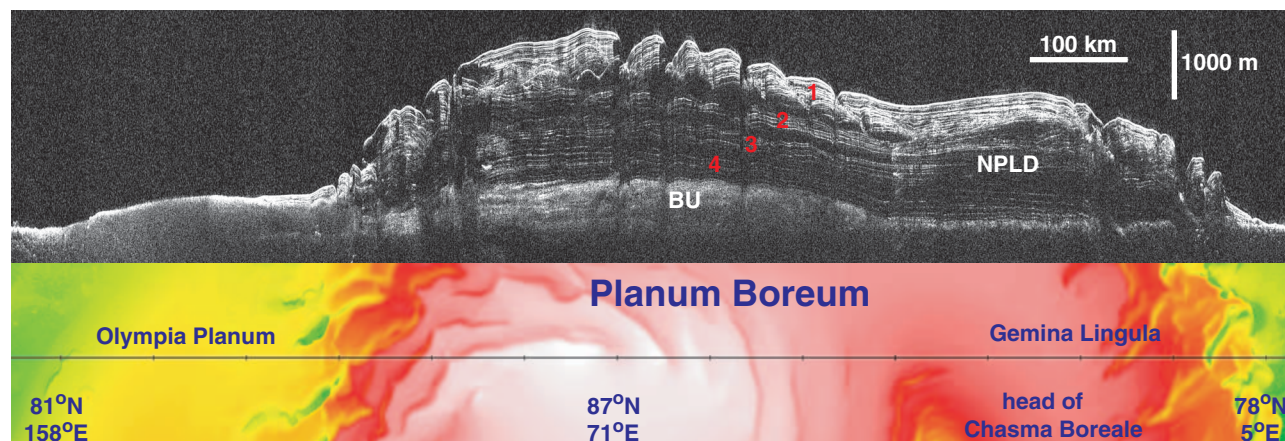

Fig. 1. (**Top**) Radargram from SHARAD orbit 5192. Range time delay, the usual ordinate in a radargram, has been converted to depth by assigning real permittivities of 1 and 3 above and below the detected ground surface, respectively. NPLD and the BU are labeled. Packet regions are numbered (see text). (**Bottom**) Ground track of orbit 5192 shown on a digital elevation model (DEM) derived from Mars Orbiter Laser Altimeter (MOLA) data. Elevation range is ~−4.5 (green) to −2 km (white).
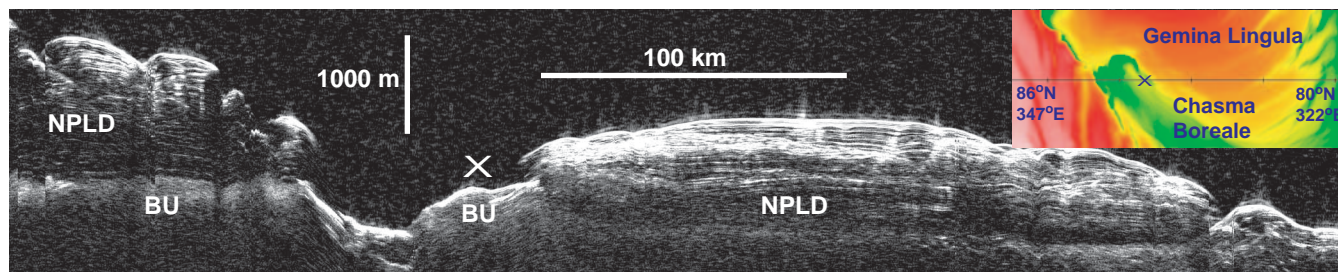

Fig. 2. Radargram from SHARAD orbit 5220 with time-to-depth algorithm applied (see Fig. 1 legend). Image contrast has been truncated to emphasize the NPLD/BU contact, so the depth extent of the BU is not apparent beneath the main portion of Planum Boreum. (**Inset**) Ground track location on MOLA DEM. The "×" marks location in radargram and on DEM of a bench of BU on the Gemina Lingula side of Chasma Boreale; the thickness of the BU rapidly terminates within Gemina Lingula.

insolation would concentrate the dust in layers (*19*). Interpacket regions could correspond to times of lows in the 2.4-My solar system dynamical resonance modulation of eccentricity that have occurred ~1.4, ~3.8, and ~6.2 Ma (*16*), with the earliest age slightly older than the calculated transition to the present LMO epoch of stable north polar ice. A second model proposes that the interpacket regions correspond to relatively low-obliquity phases at ~0.8, ~2.0, and ~3.2 Ma within the overall LMO epoch of the last 5 My. These would be times of relatively high rates of ice return to the poles within an overall net-accretion scenario (*19*). The low-obliquity scenario is perhaps more consistent with models of NPLD construction within the last 5 My (*19*), though growth rate and timing in such models depend on, among other things, assumptions regarding sublimation processes.

If the NPLD somehow survived epochs of high obliquity, each interpacket region could then represent a distinct, earlier epoch of LMO that is not predictable, as obliquity solutions become chaotic beyond 10 to 20 Ma (*23*). A problem with this hypothesis is that it does not explain the structure at the top of the NPLD column, which should be an interpacket region during the present LMO era. Instead, this section of the NPLD contains abundant reflective layers, and no interpacket region is observed with SHARAD to within its 10 to 20 m range resolution near the surface. Stratigraphic relations and geologic unit ages inferred from crater densities allow the NPLD below the uppermost several layers to range in age from a few million years to ~1 billion years (*8*), which is not a strong constraint.

Deflection of the substrate—geodynamical implications. The deflection of the substrate boundary in Gemina Lingula, where the NPLD is presumably in direct contact with the VBF, is at most 100 m (see SOM text). We used a spherical-shell loading model (*24*) to calculate deflection of the elastic lithosphere in response to the cap load (*25*), seeking the minimum value of elastic thickness, T_e, that is consistent with the 100-m value. A T_e value of 300 km satisfies this criterion

(fig. S4) and can be taken as the lower bound on T_e in this region of Mars for the current era.

This exercise can be repeated for the SPLD load, where MARSIS data have been used to effectively strip off the volume of the deposits, revealing the topography of the substrate (*26*). It is difficult to estimate a flexural signal here because the substrate consists of rugged highlands topography. There is a tendency in some longitudinal sectors for a decrease in substrate elevation from the periphery toward the center of the SPLD load, although this could be a result of large impact basins near the pole. Smooth-surface fits to the data suggest that the elevation decreases as much as ~200 to 250 m, corresponding to a lower bound on T_e of 275 to 300 km. This value could reflect solely the noise of the substrate topography, which obscures any smaller flexural signal. Independent of this work, a gravity-topography spectral estimate of the SPLD load response has yielded a T_e best-fit estimated value of 140 km, though any $T_e > 102$ km satisfies the data constraints (*27*). From the substrate deflections, the lower bound for both polar loads, ~300 km, is at least a factor of 3 higher than nearly all previous estimates of T_e on Mars (*28*).

At present, T_e estimates are essentially the only way to infer heat flow and temperatures for the martian shallow interior at points during its history. The most straightforward way to estimate these thermal parameters is to equate, for a given deflection curvature, the bending moment for a given T_e to the bending moment of an elastic-plastic lithosphere (*29*), where for the latter the temperature dependence enters through a specified viscous creep relation. To calculate the elastic-plastic bending moment, we used a relatively low basal yield stress of 10 MPa, which produces considerable strain at high temperatures in the mantle (*30*) and errs on the side of producing either higher temperatures for a given lithospheric thickness or thicker lithospheres for the same temperatures. The temperature estimate was adopted from a standard chondritic thermal model for mantle heat flux into the base of the lithosphere and crustal heat-source

enrichment (*31*); the model can be scaled up and down from its chondritic values. For a diabase crust (*32*) and an olivine mantle (*30*), a 300-km lithosphere corresponds to a wet or dry olivine mantle containing ~70 or ~80% of chondritic heat sources, respectively (see SOM text).

We tested the plausibility of this result using an inverse approach. We questioned what T_e value would be obtained if the polar loads were emplaced with the same chondritic fractions earlier in martian history (say at 3 Ga) and whether this number is consistent with T_e values obtained elsewhere on the planet for features of this age. The answer obtained for both wet and dry olivine at the same subchondritic fractions as above is $T_e \sim$ 140 km. This value is on the high side relative to most other estimates made for this epoch (*28*), although such estimates carry considerable uncertainty (*33*), and most of these T_e values arise from areas that are associated with magmatism (e.g., shield volcanoes). Subsurface heat flow has certainly been spatially heterogeneous over the history of Mars, having been anomalously high at the large magmatic centers such as Tharsis and Elysium but less than the planetary average elsewhere, including the polar regions. This is an alternative explanation to the hypothesis of planetwide subchondritic heat sources, though it may be less plausible if these volcanic regions were generated by mantle plumes (*34*) driven by core energy.

It is possible that the small amount of polar substrate deflection observed results from a transient state of the planet's interior in response to the polar loads. That is, not enough time has passed since the loads were emplaced for the deflection to reach elastic equilibrium. In that case, the 300-km bound on T_e is not a valid result; instead, the SHARAD constraint ($\leq$100-m deflection) provides information about the viscosity structure of the mantle. From the discussion above, we suggest that a lower bound on the age of the NPLD is on the order of 1 Ma, taking into account the growth time of the load. We used chondritic thermal models (*31, 35*) to set up viscoelastic loading models (*36*) and
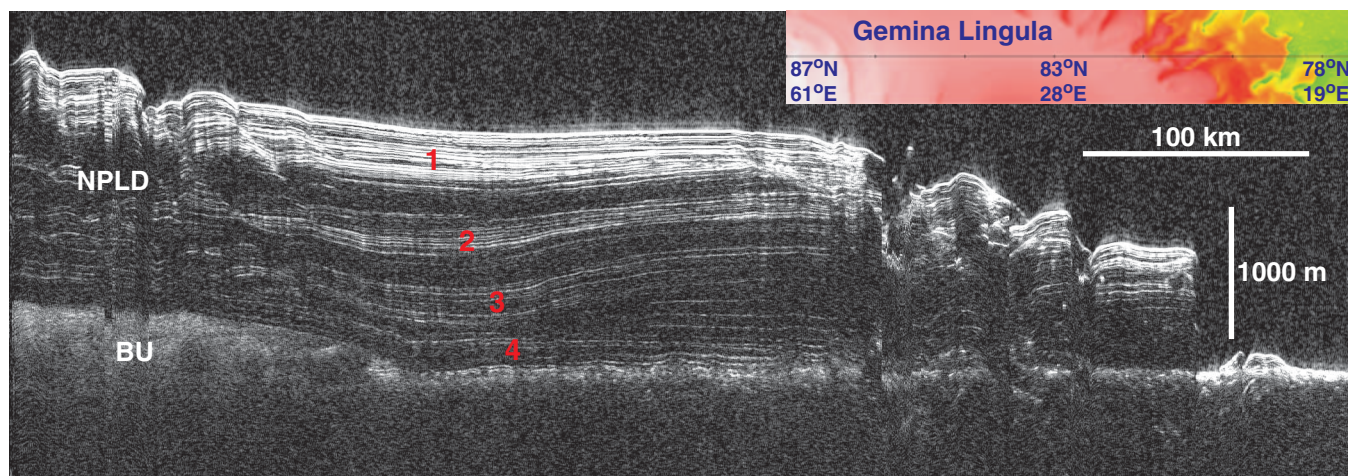

Fig. 3. Radargram from SHARAD orbit 5297 with time-to-depth algorithm applied (see Fig. 1 legend). (**Inset**) Ground track location on MOLA DEM. Packet regions are numbered (see text).

found that they generated too much deflection (see SOM text and fig. S5). This is an alternative way of arriving at the conclusion that Mars probably has subchondritic heat sources.

References and Notes

1. K. R. Blasius, J. A. Cutts, A. D. Howard, *Icarus* **50**, 140 (1982).
2. J. A. Cutts, B. H. Lewis, *Icarus* **50**, 216 (1982).
3. P. C. Thomas, S. W. Squyres, K. E. Herkenhoff, A. D. Howard, B. C. Murray, in *Mars*, H. H. Kieffer, B. M. Jakosky, C. W. Snyder, M. S. Matthews, Eds. (Univ. of Arizona Press, Tucson, AZ, 1992), pp. 767–795.
4. M. C. Malin, K. S. Edgett, *J. Geophys. Res.* **106**, 23429 (2001).
5. K. E. Fishbaugh, J. W. Head, *Icarus* **174**, 444 (2005).
6. S. Byrne, B. C. Murray, *J. Geophys. Res.* **107**, 5044 (2002).
7. K. S. Edgett, R. M. E. Williams, M. C. Malin, B. A. Cantor, P. C. Thomas, *Geomorphology* **52**, 289 (2003).
8. K. L. Tanaka *et al.*, *Icarus*, published online 29 February 2008; 10.1016/j.icarus.2008.01.021.
9. K. E. Herkenhoff, S. Byrne, P. S. Russell, K. E. Fishbaugh, A. S. McEwen, *Science* **317**, 1711 (2007).
10. Features in the radargram beneath the troughs may or may not be real structures. The discontinuities in reflections might arise, for example, from poor radar-signal penetration because of surface scattering from the trough floors.
11. G. Picardi *et al.*, *Science* **310**, 1925 (2005), published online 29 November 2005; 10.1126/science.1122165.
12. W. M. Calvin *et al.*, *Lunar Planet. Sci.* **XXXIX**, 1939 (abstr.) (2008).
13. Y. Langevin *et al.*, *Science* **307**, 1581 (2005), published online 17 February 2005; 10.1126/science.1109438.
14. M. T. Zuber *et al.*, *Science* **317**, 1718 (2007).
15. D. C. Nunes, R. J. Phillips, *J. Geophys. Res.* **111**, E06S21 (2006).
16. J. Laskar, B. Levrard, J. F. Mustard, *Nature* **419**, 375 (2002).
17. The climate precession is the insolation effect of the precession of the spin axis modulated by the orbital eccentricity. The result is that the calendar date of perihelion precesses.
18. M. T. Mellon, B. M. Jakosky, *J. Geophys. Res.* **100**, 11781 (1995).
19. B. Levrard, F. Forget, F. Montmessin, J. Laskar, *J. Geophys. Res.* **112**, E06012 (2007).
20. S. M. Milkovich, J. W. Head III, *J. Geophys. Res.* **110**, E01005 (2005).
21. R. M. Haberle, J. R. Murphy, J. Schaeffer, *Icarus* **161**, 66 (2003).
22. O. B. Toon, J. B. Pollack, W. Ward, J. A. Burns, K. Bilski, *Icarus* **44**, 552 (1980).
23. J. Laskar *et al.*, *Icarus* **170**, 343 (2004).
24. W. B. Banerdt, *J. Geophys. Res.* **91**, 403 (1986).
25. C. L. Johnson *et al.*, *Icarus* **144**, 313 (2000).
26. J. J. Plaut *et al.*, *Science* **316**, 92 (2007), published online 14 March 2007; 10.1126/science.1139672.
27. M. A. Wieczorek, *Icarus*, published online 10 January 2008; 10.1016/j.icarus.2007.10.026.
28. M. Grott, D. Breuer, *Icarus* **193**, 503 (2008).
29. M. K. McNutt, *J. Geophys. Res.* **89**, 11180 (1984).
30. S.-i. Karato, P. Wu, *Science* **260**, 771 (1993).
31. S. A. Hauck II, R. J. Phillips, *J. Geophys. Res.* **107**, 5052 (2002).
32. Y. Caristan, *J. Geophys. Res.* **87**, 6781 (1982).
33. V. Belleguic, P. Lognonné, M. Wieczorek, *J. Geophys. Res.* **110**, E11005 (2005).
34. C. L. Johnson, R. J. Phillips, *Earth Planet. Sci. Lett.* **230**, 241 (2005).
35. D. Breuer, T. Spohn, *J. Geophys. Res.* **108**, 5072 (2003).
36. P. S. Mohit, R. J. Phillips, *J. Geophys. Res.* **111**, E12001 (2006).
37. SHARAD was provided by the Italian Space Agency, and its operations are led by Dipartimento InfoCom, Università di Roma "La Sapienza." Thales Alenia Space Italia is the prime contractor for SHARAD. The Mars Reconnaissance Orbiter mission is managed by the Jet Propulsion Laboratory, California Institute of Technology, for the NASA Science Mission Directorate, Washington, DC. Lockheed Martin Space Systems, Denver, CO, is the prime contractor for the orbiter. We thank three anonymous reviewers for very constructive comments. S. Hauck provided very useful advice.

Widespread Translational Inhibition by Plant miRNAs and siRNAs

Peter Brodersen,[1] Lali Sakvarelidze-Achard,[1] Marianne Bruun-Rasmussen,[1] Patrice Dunoyer,[1] Yoshiharu Y. Yamamoto,[2] Leslie Sieburth,[3] Olivier Voinnet[1]*

High complementarity between plant microRNAs (miRNAs) and their messenger RNA targets is thought to cause silencing, prevalently by endonucleolytic cleavage. We have isolated *Arabidopsis* mutants defective in miRNA action. Their analysis provides evidence that plant miRNA–guided silencing has a widespread translational inhibitory component that is genetically separable from endonucleolytic cleavage. We further show that the same is true of silencing mediated by small interfering RNA (siRNA) populations. Translational repression is effected in part by the ARGONAUTE proteins AGO1 and AGO10. It also requires the activity of the microtubule-severing enzyme katanin, implicating cytoskeleton dynamics in miRNA action, as recently suggested from animal studies. Also as in animals, the decapping component VARICOSE (VCS)/Ge-1 is required for translational repression by miRNAs, which suggests that the underlying mechanisms in the two kingdoms are related.

MicroRNAs are 20- to 24-nucleotide (nt) RNAs that regulate eukaryotic gene expression posttranscriptionally. Bound to ARGONAUTE (AGO) proteins, miRNAs guide RNA-induced silencing complexes (RISCs) to partly or fully complementary mRNAs (*1*). Two modes of negative regulation by RISC exist: (i) translational repression, sometimes coupled to accelerated mRNA decay, and (ii) RISC-catalyzed endonucleolytic mRNA cleavage ("slicing"). The degree of miRNA-mRNA complementarity is a key determinant of the mechanism used, such that perfect complementarity enables cleavage, whereas central mismatches exclude slicing to promote translational repression (*2*, *3*). Unlike most animal miRNAs, most plant miRNAs show near-perfect or perfect complementarity to their targets, and slicing is believed to be their predominant, or exclusive, mode of action (*4*). Accordingly, *Arabidopsis* AGO1 binds

miRNAs and displays slicer activity toward miRNA targets, and strong *ago1* loss-of-function mutants overaccumulate miRNA target transcripts (*5–7*). Nonetheless, many questions regarding miRNA-RISC composition, loading, and target identification persist, mostly because AGO1 remains the only factor known to be implicated in plant miRNA action. It is also unclear whether near-perfect complementarity within plant miRNA–target pairs actually excludes translational inhibition, as is commonly inferred, or whether it allows slicing to occur in addition to translational inhibition.

To address these issues, we carried out a forward genetic screen for *Arabidopsis* mutants defective in silencing of a constitutively expressed green fluorescent protein (GFP) mRNA containing a miR171 target site immediately downstream of the stop codon (Fig. 1A) (*8*). In seedlings, GFP is silenced by endogenous miR171, except in the vasculature and in the roots where miR171 ex-

pression is low (*8*). Twenty-one recessive mutants defective in miR171-guided silencing were identified by gain of GFP expression in leaves (Fig. 1B); none had mutations in the miR171 target site. Eight nonallelic mutants showing consistently higher GFP expression than the parental line GFP171.1 [wild type (WT)] after two backcrosses (fig. S1) were studied in further detail.

***mbd* and *mad* mutants.** Two mutants (class I) had strongly reduced levels of several miRNAs and were referred to as *microRNA biogenesis deficient* (*mbd1* and *mbd2*) (fig. S1 and Fig. 1C). miRNA biogenesis in *Arabidopsis* involves processing of primary miRNA transcripts by a nuclear-localized complex of DICER-LIKE1 (DCL1), the double-stranded RNA binding protein HYL1, and the zinc finger protein SE. Excised miRNA/miRNA* duplexes are then stabilized through HEN1-catalyzed 2′-O-methylation [reviewed in (*9*)]. A G-to-A transition in *mbd1* (renamed *dcl1-12*) disrupts a splice donor site in the *DCL1* gene, which strongly reduces the accumulation of correctly spliced DCL1 mRNA (fig. S1). *mbd2* (renamed *hen1-7*) has a missense mutation resulting in a Gly-to-Glu change in the HEN1 *S*-adenosyl methionine–binding motif, which is predicted to abolish small RNA methylation (fig. S1). The remaining six mutants exhibited normal miRNA levels and were classified as *microRNA action deficient mad1* to *mad6* (Fig. 1C). *mad1* to *mad6* showed low miR160*

[1]Institut de Biologie Moléculaire des Plantes du CNRS, Unité Propre de Recherche 2357, 12 rue du Général Zimmer, 67084 Strasbourg Cedex, France. [2]Center for Gene Research, Nagoya University, Furo-cho, Chikusa-ku, Nagoya Aichi, 464-8602, Japan. [3]Department of Biology, University of Utah, Salt Lake City, UT 84112, USA.

*To whom correspondence should be addressed. E-mail: olivier.voinnet@ibmp-ulp.u-strasbg.fr